

# Epitaxial Synthesis of Monolayer PtSe<sub>2</sub> Single Crystal on MoSe<sub>2</sub> with Strong Interlayer Coupling

Jiadong Zhou,<sup>†,•</sup> Xianghua Kong,<sup>‡,§,•</sup> Chandra Mutyala,<sup>||,⊥,•</sup> Junhao Lin,<sup>\*,#</sup> Frederic Le Goualher,<sup>†</sup> Rui Xu,<sup>§,∇</sup> Xiaowei Wang,<sup>†</sup> Yu Chen,<sup>○</sup> Yao Zhou,<sup>○</sup> Chao Zhu,<sup>†</sup> Wei Lu,<sup>||,⊥</sup> Fucai Liu,<sup>†</sup> Bijun Tang,<sup>†</sup> Zenglong Guo,<sup>#</sup> Chao Zhu,<sup>†</sup> Zhihai Cheng,<sup>§,∇</sup> Ting Yu,<sup>○</sup> Kazu Suenaga,<sup>◆</sup> Dong Sun,<sup>\*,||,⊥</sup> Wei Ji,<sup>\*,§</sup> and Zheng Liu<sup>\*,†,||</sup>

<sup>†</sup>School of Materials Science and Engineering, Nanyang Technological University, 639798 Singapore

<sup>‡</sup>Department of Physics and Centre for the Physics of Materials, McGill University, Montreal, Quebec H3A 2T8, Canada

<sup>§</sup>Department of Physics and Beijing Key Laboratory of Optoelectronic Functional Materials and Micro-nano Devices, Renmin University of China, Beijing 100872, China

<sup>||</sup>International Center for Quantum Materials, School of Physics, Peking University, Beijing 100871, China

<sup>⊥</sup>Collaborative Innovation Center of Quantum Matter, Beijing 100871, China

<sup>#</sup>Department of Physics, Southern University of Science and Technology, Shenzhen 518055, China

<sup>∇</sup>CAS Key Laboratory of Standardization and Measurement for Nanotechnology, CAS Center for Excellence in Nanoscience, National Center for Nanoscience and Technology, Beijing 100190, China

<sup>○</sup>Centre for Disruptive Photonic Technologies, School of Physical and Mathematical Sciences, Nanyang Technological University, 637371 Singapore

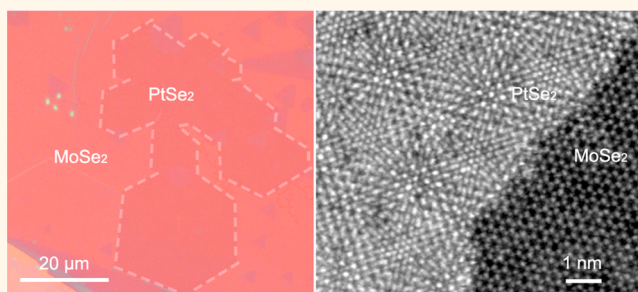
<sup>◆</sup>National Institute of Advanced Industrial Science and Technology (AIST), Tsukuba 305-8565, Japan

<sup>||</sup>CNRS International NTU THALES Research Alliances, UMI 3288, Research Techno Plaza, 50 Nanyang Drive, Border X Block, Level 6, 637553 Singapore

**S** Supporting Information

**ABSTRACT:** PtSe<sub>2</sub>, a layered two-dimensional transition-metal dichalcogenide (TMD), has drawn intensive attention owing to its layer-dependent band structure, high air stability, and spin-layer locking effect which can be used in various applications for next-generation optoelectronic and electronic devices or catalysis applications. However, synthesis of PtSe<sub>2</sub> is highly challenging due to the low chemical reactivity of Pt sources. Here, we report the chemical vapor deposition of monolayer PtSe<sub>2</sub> single crystals on MoSe<sub>2</sub>. The periodic Moiré patterns from the vertically stacked heterostructure (PtSe<sub>2</sub>/MoSe<sub>2</sub>) are clearly identified *via* annular dark-field scanning transmission electron microscopy. First-principles calculations show a type II band alignment and reveal interface states originating from the strong–weak interlayer coupling (SWIC) between PtSe<sub>2</sub> and MoSe<sub>2</sub> monolayers, which is supported by the electrostatic force microscopy imaging. Ultrafast hole transfer between PtSe<sub>2</sub> and MoSe<sub>2</sub> monolayers is observed in the PtSe<sub>2</sub>/MoSe<sub>2</sub> heterostructure, matching well with the theoretical results. Our study will shed light on the synthesis of Pt-based TMD heterostructures and boost the realization of SWIC-based optoelectronic devices.

**KEYWORDS:** PtSe<sub>2</sub>, PtSe<sub>2</sub>/MoSe<sub>2</sub> heterostructure, two-dimensional material, chemical vapor deposition, interlayer coupling



Platinum diselenide (PtSe<sub>2</sub>) is an intriguing layered material due to its helical spin texture induced by local Rashba effect<sup>1</sup> and strong interlayer coupling.<sup>2,3</sup> Recent work also revealed that the strong interlayer coupling can

**Received:** December 15, 2018

**Accepted:** September 24, 2019

**Published:** September 24, 2019

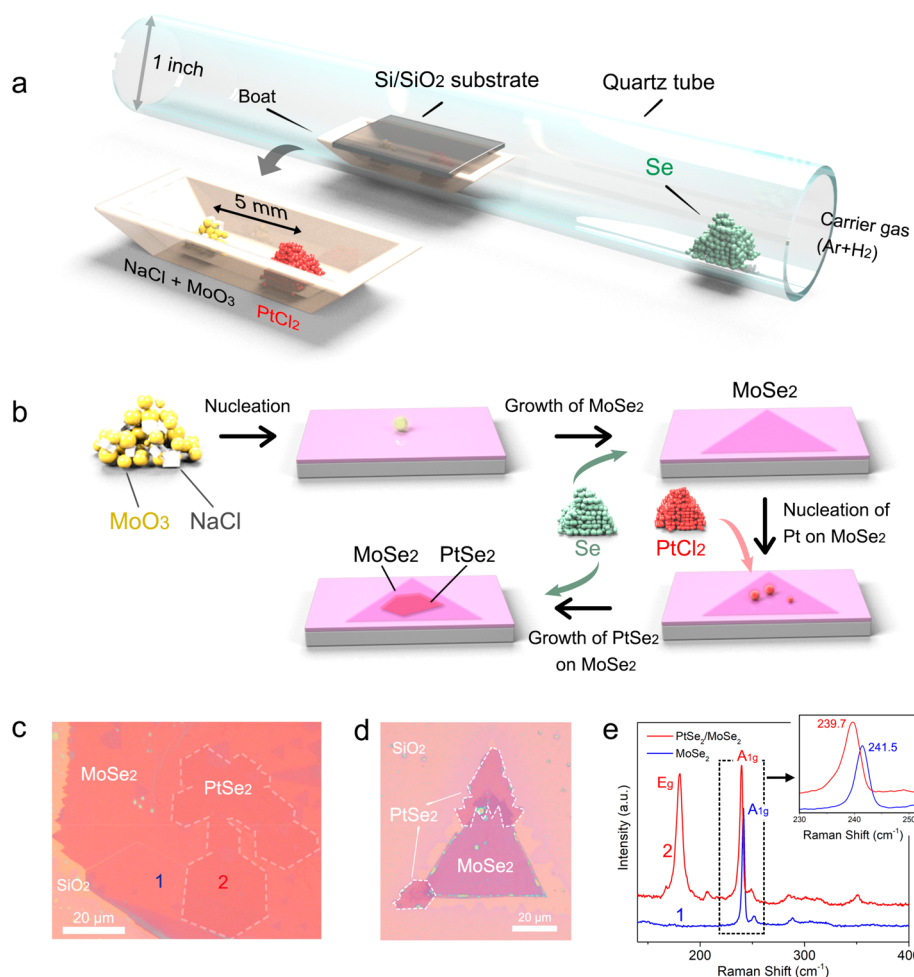


**Figure 1.** Reaction system and spectroscopy characterizations of PtSe<sub>2</sub>/MoSe<sub>2</sub> vertical heterostructures. (a) Reaction system used to synthesize PtSe<sub>2</sub> and PtSe<sub>2</sub>/MoSe<sub>2</sub> vertical heterostructure and the atomic crystal structure of PtSe<sub>2</sub>/MoSe<sub>2</sub>. (b) Growth mechanism of PtSe<sub>2</sub>/MoSe<sub>2</sub> heterostructure. (c and d) Optical images of as-synthesized PtSe<sub>2</sub>/MoSe<sub>2</sub> heterostructure with different styles. From the optical images, the size of the overlapped vertical heterostructure is about 40 μm, and the area of the vertical heterostructure is larger than 1000 μm<sup>2</sup>. (e) The Raman spectra in the positions 1 and 2 of the heterostructure (inset shows the optical image of the vertical heterostructure). The A<sub>1g</sub> mode located at 240 cm<sup>-1</sup> confirms that the crystal is MoSe<sub>2</sub>. The Raman peaks located at 175 and 205 cm<sup>-1</sup> originate from the E<sub>g</sub> mode of PtSe<sub>2</sub>. The Raman peaks located at 240 cm<sup>-1</sup> can be contributed to the A<sub>1g</sub> vibration mode of MoSe<sub>2</sub>. These indicate that the as-synthesized PtSe<sub>2</sub> and MoSe<sub>2</sub> form the vertical heterostructure. Notably, the A<sub>1g</sub> mode of MoSe<sub>2</sub> from the PtSe<sub>2</sub>/MoSe<sub>2</sub> heterostructure shows a little shift due to the coupling between PtSe<sub>2</sub> and MoSe<sub>2</sub>.

45 induce a PtSe<sub>2</sub> transition from a semimetal (bulk) to a  
 46 semiconductor (monolayer) with a band gap increasing from 0  
 47 to 1.2 eV.<sup>4,5</sup> The narrow bandgap of few layer PtSe<sub>2</sub> renders it  
 48 an excellent candidate for broadband mid-infrared detec-  
 49 tors.<sup>3,6,7</sup> Furthermore, field-effect transistors (FETs) based on  
 50 few-layer PtSe<sub>2</sub> display high mobility and good stability in air.<sup>5</sup>  
 51 All these fascinating results indicate that PtSe<sub>2</sub> can be an  
 52 attractive candidate for various applications in electronic and  
 53 optoelectronic devices.<sup>8</sup> Therefore, controlled synthesis of  
 54 high-quality and atomically thin PtSe<sub>2</sub> layers is urgently  
 55 required. So far, the mechanical exfoliation has been widely  
 56 adopted to produce PtSe<sub>2</sub> monolayers. However, this method  
 57 is low yield and time-consuming and usually leads to small size  
 58 PtSe<sub>2</sub> flakes. Although few-layered PtSe<sub>2</sub> can be synthesized by  
 59 selenization of Pt films or molecular beam epitaxy (MBE),<sup>9–12</sup>  
 60 synthesis of large size monolayer PtSe<sub>2</sub> single crystals is yet to  
 61 be achieved, due to the low chemical reactivity of Pt.<sup>1,2,12,13</sup>  
 62 Here, we demonstrate the synthesis of monolayer PtSe<sub>2</sub>  
 63 using the chemical vapor deposition (CVD) method. Various  
 64 substrates including SiO<sub>2</sub>/Si, Al<sub>2</sub>O<sub>3</sub>, and MoSe<sub>2</sub> have been

used for the growth of PtSe<sub>2</sub>. It is found that PtSe<sub>2</sub> monolayers  
 65 can only be epitaxially grown on MoSe<sub>2</sub> substrate, forming a  
 66 PtSe<sub>2</sub>/MoSe<sub>2</sub> vertical heterostructure. Such structure is  
 67 confirmed by the Moiré fringe from annular dark-field scanning  
 68 transmission electron microscopy (ADF-STEM). First-princi-  
 69 ples calculations show that the formed heterostructure has a  
 70 direct band gap and forms a type II band alignment. A more  
 71 striking result lies in the emergence of interface states located  
 72 within the original bandgap. These states are hybridized by the  
 73 wave functions of Se-p<sub>z</sub> and Pt/Mo-d<sub>z</sub><sup>2</sup> orbitals from the PtSe<sub>2</sub>  
 74 monolayer and MoSe<sub>2</sub> monolayer whose intrinsic interlayer  
 75 couplings are strong and weak, respectively, in their own  
 76 multilayers. The edge states of PtSe<sub>2</sub> on MoSe<sub>2</sub> observed with  
 77 electrostatic force microscopy (EFM) compellingly support the  
 78 existence of the theoretically predicted interface states. The  
 79 charge transfer from PtSe<sub>2</sub> to MoSe<sub>2</sub> probed by ultrafast  
 80 electron dynamics further demonstrates the interlayer coupling  
 81 and band alignment in the PtSe<sub>2</sub>/MoSe<sub>2</sub> heterostructure. Our  
 82 work is helpful toward the synthesis of a PtSe<sub>2</sub> monolayer and 83

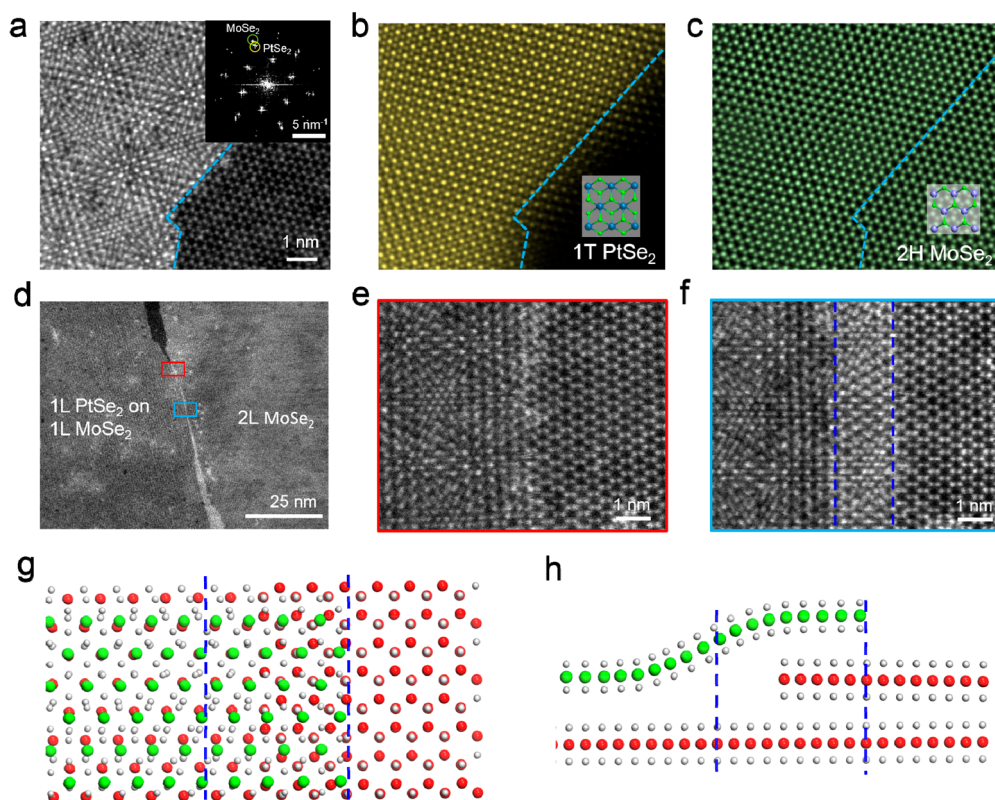


**Figure 2.** Atomic structure of the vertically stacked PtSe<sub>2</sub>/MoSe<sub>2</sub> heterostructure and lateral boundary. (a) Experimental atomic-resolution ADF-STEM image of PtSe<sub>2</sub>/MoSe<sub>2</sub>, showing the periodic Moiré pattern where the monolayer PtSe<sub>2</sub> stacks on top of monolayer MoSe<sub>2</sub>. Inset shows the FFT pattern obtained from (a), where the lattice constants of 0.376 and 0.332 nm correspond to the lattice of PtSe<sub>2</sub> and MoSe<sub>2</sub>, as highlighted by the yellow and green circles, respectively. (b and c) Inverse FFT image of (a) by selectively filtering out the PtSe<sub>2</sub> (b) and MoSe<sub>2</sub> (c) lattice information in the FFT pattern, respectively. The 1T phase of PtSe<sub>2</sub> and 1H phase of MoSe<sub>2</sub> are confirmed by their discrete contrast which are consistent with the overlaid atomic models. (d) Low-magnification STEM image of the lateral boundary in a bilayer region. The left part is the PtSe<sub>2</sub>/MoSe<sub>2</sub> heterostructure, while the right part is bilayer MoSe<sub>2</sub>. (e and f) Atomic-resolution images of the highlighted regions in (d), showing the initial stage (e) and the overlapping region (f) of the lateral boundary. The initial stage shows a sharp change from PtSe<sub>2</sub> to MoSe<sub>2</sub> lattice with some tiny regions of bright contrast along the edge, indicating both PtSe<sub>2</sub> and MoSe<sub>2</sub> lattices have a sharp edge termination without any chemical bonding. The PtSe<sub>2</sub> and MoSe<sub>2</sub> gradually overlapped with each other along the boundary. (g and h) The top (g) and side (h) views of the schematic atomic models of the overlapping lateral boundary.

84 demonstrates its potential in electronic and optoelectronic  
85 devices.

## 86 RESULTS AND DISCUSSION

87 Herein, the epitaxial growth of PtSe<sub>2</sub> on MoSe<sub>2</sub> was achieved  
88 by using PtCl<sub>2</sub> and MoO<sub>3</sub>/NaCl mixed powders as sources.<sup>14</sup>  
89 More information about the growth is provided in the  
90 Methods section. Figure 1a illustrates the reaction system for  
91 the growth of PtSe<sub>2</sub> crystals. Figure 1b shows the proposed  
92 growing mechanism. Monolayer PtSe<sub>2</sub> single crystals were  
93 obtained on a MoSe<sub>2</sub> substrate with a one-step CVD method,  
94 as shown in Figure 1c,d. Generally, most of the as-grown  
95 samples were vertically stacked PtSe<sub>2</sub>/MoSe<sub>2</sub>. We believe that  
96 the large lattice mismatch between PtSe<sub>2</sub> and MoSe<sub>2</sub> (1T for  
97 PtSe<sub>2</sub> and 1H for MoSe<sub>2</sub>) hinders the epitaxial growth of PtSe<sub>2</sub>  
98 and MoSe<sub>2</sub> in-plane heterostructure. Figure 1c shows the  
99 hexagonal PtSe<sub>2</sub> monolayers atop the MoSe<sub>2</sub> monolayer with a  
100 lateral size of ~30 μm. Such size is much larger than the  
101 previously reported value.<sup>13</sup> Atomic force microscopy (AFM)  
102 was conducted to determine the height of the as-prepared  
103 PtSe<sub>2</sub>/MoSe<sub>2</sub> heterostructure. The thickness of PtSe<sub>2</sub> is ~0.8  
104 nm, confirming its monolayer nature (Figure S1). More optical  
105 images along with the size distribution of PtSe<sub>2</sub> flakes are  
106 provided in Figure S2. The second layer MoSe<sub>2</sub> which coexists

with monolayer PtSe<sub>2</sub> can also be found in some synthesized  
107 samples. The area of the PtSe<sub>2</sub>/MoSe<sub>2</sub> heterostructure (Figure  
108 1c) can be up to ~1000 μm<sup>2</sup>. The size comparison is shown in  
109 Figure S3.<sup>15–22</sup> Meanwhile, we also observed that PtSe<sub>2</sub>  
110 monolayers can grow not only epitaxially on top of MoSe<sub>2</sub>  
111 but also partially overlap with MoSe<sub>2</sub> due to the different  
112 growing rates of PtSe<sub>2</sub> and MoSe<sub>2</sub>, as shown in Figure 1d. This  
113 should be attributed to the nucleation formation of PtSe<sub>2</sub> on  
114 the edge of MoSe<sub>2</sub>, which then grows outward (down the  
115 step). The Raman spectrum and thickness of PtSe<sub>2</sub> with a  
116 similar morphology is shown in Figure S4.  
117

In order to demonstrate the role of MoSe<sub>2</sub>, time-dependent  
118 experiments were carried out. For a short growing time (3  
119 min), only MoSe<sub>2</sub> can be observed. By increasing the growing  
120 time to 10 min, the PtSe<sub>2</sub>/MoSe<sub>2</sub> heterostructure can be  
121 obtained (see Figure S5). We also used different substrates  
122 including exfoliated MoSe<sub>2</sub> flakes, SiO<sub>2</sub>/Si, and sapphire wafers  
123 to synthesize PtSe<sub>2</sub> crystals. Only PtSe<sub>2</sub> thick flakes and  
124 particles can be obtained on exfoliated MoSe<sub>2</sub> flakes (Figure  
125 S6). For SiO<sub>2</sub>/Si and sapphire substrates, at the growing  
126 temperature of ~400 °C, only polycrystalline PtSe<sub>2</sub> films can  
127 be obtained (Figure S7). Increasing the growing temperature  
128 to ~810 °C will result in few-layer PtSe<sub>2</sub> single crystal (Figures  
129 S8 and S9). These results are consistent with previous reports  
130

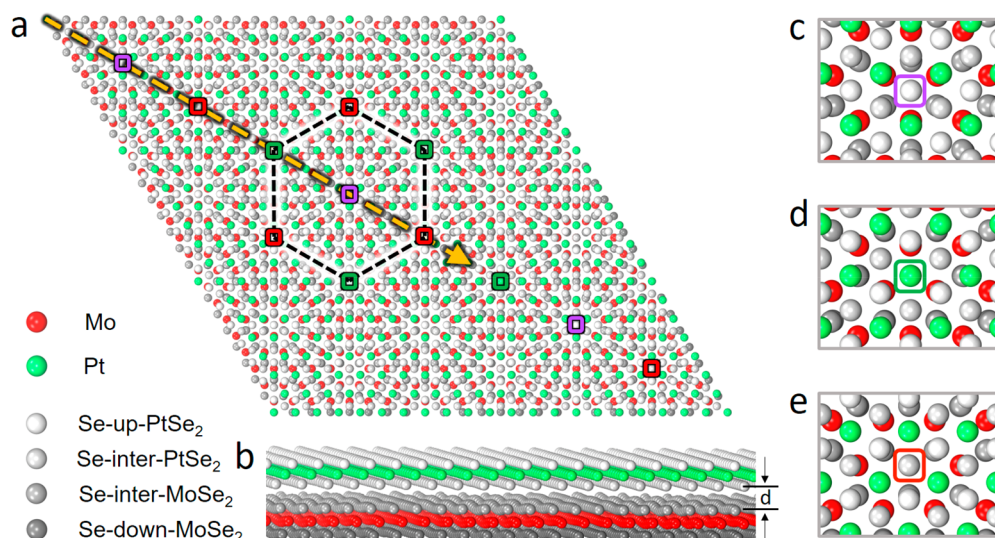


**Figure 3.** Geometry information on PtSe<sub>2</sub>(1T)/MoSe<sub>2</sub>(1H) vertical heterostructures. (a and b) Top and side views of the geometry structure of PtSe<sub>2</sub>(1T)/MoSe<sub>2</sub>(1H) vertical heterostructures. The violet, green, and red rectangles denote three high-symmetry stacking local configurations which have been zoomed in in (c) Se<sub>inter</sub>(PtSe<sub>2</sub>)-Se<sub>inter</sub>(MoSe<sub>2</sub>) stacking, (d) Pt-Se<sub>inter</sub>(MoSe<sub>2</sub>) stacking, and (e) Se<sub>inter</sub>(PtSe<sub>2</sub>)-Mo stacking, respectively. And parameter *d* marked in (b) refers to the interlayer distance between PtSe<sub>2</sub>(1T) and MoSe<sub>2</sub>(1H).

131 on the growth of PtSe<sub>2</sub> flakes on MoSe<sub>2</sub>.<sup>9,13</sup> Based on these  
132 results, it can be concluded that the CVD-grown MoSe<sub>2</sub>  
133 monolayer is a good candidate for the epitaxial growth of  
134 PtSe<sub>2</sub> monolayer.

135 The successful growth of PtSe<sub>2</sub> monolayer on MoSe<sub>2</sub> can be  
136 attributed to the following two reasons: (1) The chemical  
137 reactivity between Mo precursors and Se is higher than that  
138 between Pt precursor and Se and the vapor pressure of Mo  
139 precursors is relatively higher than that of Pt precursor.<sup>14</sup> As a  
140 result, the growing rate of MoSe<sub>2</sub> is faster than that of PtSe<sub>2</sub>,  
141 which makes MoSe<sub>2</sub> grow first. (2) The lattice mismatch  
142 between PtSe<sub>2</sub> and MoSe<sub>2</sub> is smaller than that between PtSe<sub>2</sub>  
143 and SiO<sub>2</sub>/Si (or Al<sub>2</sub>O<sub>3</sub>). Therefore, MoSe<sub>2</sub> is a favorable  
144 substrate for the epitaxial growth of PtSe<sub>2</sub> monolayer  
145 (comparison is provided in Table S1). We also noticed that,  
146 at a relatively high growing temperature (~810 °C), MoSe<sub>2</sub>  
147 flakes could be etched by H<sub>2</sub>, which will result in MoSe<sub>2</sub> flakes  
148 with different geometries.

149 Raman spectroscopy was carried out to investigate the  
150 structure and quality of formed PtSe<sub>2</sub>/MoSe<sub>2</sub> heterostructures.  
151 Figure 1e shows the Raman spectra collected from points 1  
152 and 2 of the sample shown in Figure 1c. The sole peak located  
153 at 240 cm<sup>-1</sup> from point 1 (blue curve) corresponds to the A<sub>1g</sub>  
154 mode of MoSe<sub>2</sub>.<sup>23</sup> Raman peaks sitting at 175, 205, and 240  
155 cm<sup>-1</sup> were collected from point 2 (red curve), corresponding  
156 to the E<sub>g</sub> and A<sub>1g</sub> modes of PtSe<sub>2</sub><sup>24</sup> and the A<sub>1g</sub> mode of  
157 MoSe<sub>2</sub>, respectively. Notably, the A<sub>1g</sub> mode of MoSe<sub>2</sub> in the  
158 PtSe<sub>2</sub>/MoSe<sub>2</sub> heterostructure shows a red shift due to the  
159 interlayer coupling between PtSe<sub>2</sub> and MoSe<sub>2</sub>, which is  
160 consistent with the experimental observations reported result<sup>11</sup>  
161 and theoretical results.<sup>25</sup> Interestingly, from point 2, a Raman  
162 peak located at ~350 cm<sup>-1</sup> can be found, which could be  
163 attributed to the interlayer coupling between PtSe<sub>2</sub> and  
164 MoSe<sub>2</sub>.<sup>26</sup> These results confirm the vertically stacked PtSe<sub>2</sub>/  
165 MoSe<sub>2</sub> heterojunction. Next, we employed X-ray photo-  
166 electron spectroscopy (XPS) to examine the composition of  
167 the PtSe<sub>2</sub>/MoSe<sub>2</sub> heterostructures. Based on XPS data (Figure  
168 S10), the atomic ratio between Se and Pt/Mo is estimated to

be ~1.97, which is very close to the stoichiometry of MoSe<sub>2</sub> 169  
and PtSe<sub>2</sub>. More information about the PL spectra and PL and 170  
Raman mappings of PtSe<sub>2</sub>/MoSe<sub>2</sub> heterostructures is presented in 171  
Figure S11. Note that the weak PL intensity of PtSe<sub>2</sub>/MoSe<sub>2</sub> 172  
heterostructures probably results from the charge 173  
transfer between PtSe<sub>2</sub> and MoSe<sub>2</sub>. 174

ADF-STEM was used to investigate the atomic structure of 175  
PtSe<sub>2</sub>/MoSe<sub>2</sub> heterostructures. Figure 2a shows the atomic- 176  
resolution ADF-STEM image of PtSe<sub>2</sub>/MoSe<sub>2</sub>. The periodic 177  
Moiré patterns can be clearly observed along the basal plane of 178  
the heterostructure, which is caused by the interference from 179  
the lattice of monolayer PtSe<sub>2</sub> and MoSe<sub>2</sub>. The fast Fourier 180  
transformation (FFT) of the PtSe<sub>2</sub>/MoSe<sub>2</sub> is shown in the 181  
inset of Figure 2a. Two different sets of diffraction patterns 182  
close to each other were identified. The lattice constants of 183  
~0.38 nm and ~0.33 nm correspond to PtSe<sub>2</sub> and MoSe<sub>2</sub> 184  
respective lattices, indicating the as-synthesized PtSe<sub>2</sub> and 185  
MoSe<sub>2</sub> are single crystals. This is further confirmed by the 186  
selected area electron diffraction pattern collected on a much 187  
larger region of PtSe<sub>2</sub>/MoSe<sub>2</sub> (over ~5 μm in size), as shown 188  
in Figure S12, which only displays one set of diffraction pattern 189  
of PtSe<sub>2</sub> and MoSe<sub>2</sub>, respectively. Moreover, the two 190  
monolayer lattices are well aligned with each other, which is 191  
a strong evidence of the vertically epitaxial growth. The FFT 192  
(inset in Figure 2a) does not show the superlattice periodicity, 193  
which is expected near the central bright spot, presumably due to 194  
its weak signal. However, the periodicity of the Moiré 195  
pattern can be directly measured in the atomically resolved 196  
image by filtering out the lattice of PtSe<sub>2</sub> and MoSe<sub>2</sub> (see 197  
Figure S13 for more details), which is estimated to be ~2.60 198  
nm. Such a large supercell indicates the highly epitaxial feature 199  
as a result of the coupling growth between the two materials. 200  
Figure 2b,c shows the inverse FFT images of Figure 2a, which 201  
distinguishes the atomic structures of the 1T and 1H phases in 202  
PtSe<sub>2</sub> and MoSe<sub>2</sub>, respectively. 203

Figure 2d shows a low magnification ADF-STEM image of 204  
the lateral boundary in the PtSe<sub>2</sub>/MoSe<sub>2</sub> heterostructure. The 205  
optical image of a similar structure is shown in Figure S14. The 206

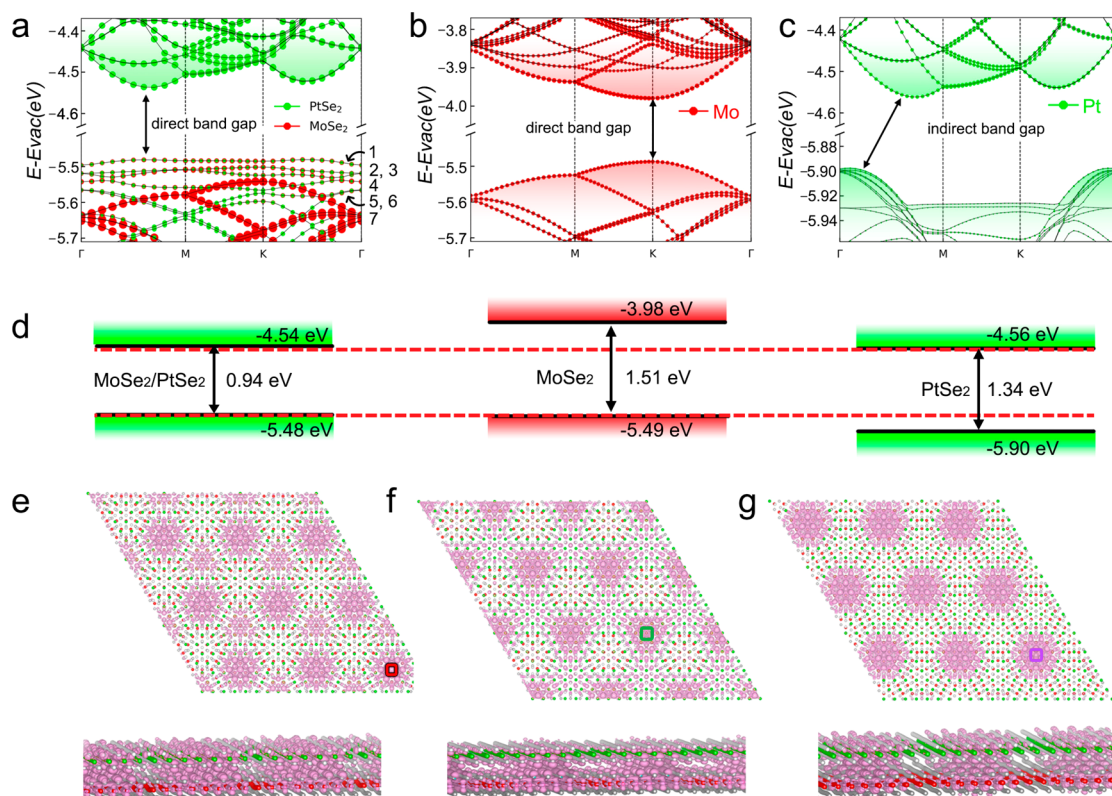


**Figure 4.** Band alignment and Spatial structures of wave functions for PtSe<sub>2</sub>(1T)/MoSe<sub>2</sub>(1H) vertical heterostructures. (a) The band structure of PtSe<sub>2</sub>(1T)/MoSe<sub>2</sub>(1H) vertical heterostructure as well as projected contributions of the marked systems. (b and c) Band structures and projected contributions of the marked atoms of deformed monolayer MoSe<sub>2</sub> and PtSe<sub>2</sub> whose geometry structures are extracted from the relaxed heterostructure. (d) Band alignment of original monolayer MoSe<sub>2</sub> and PtSe<sub>2</sub> and relaxed PtSe<sub>2</sub>(1T)/MoSe<sub>2</sub>(1H) vertical heterostructure. All energies here take the vacuum level as a reference. (e–g) Top and side views of the spatial distribution of modular squared wave functions for the marked bands 1, 4, and 7 in (a), separately. The violet, green, and red rectangles correspond to those in Figure 3. Side views display clearly each type of atom contribution to a certain band.

207 underneath MoSe<sub>2</sub> layer is continuous, thus such structure can  
 208 be considered as a grain boundary between PtSe<sub>2</sub> and MoSe<sub>2</sub>  
 209 monolayers on the MoSe<sub>2</sub> substrate. Figure 2e,f shows  
 210 atomically resolved images of two different regions along the  
 211 lateral boundaries. In fact, because of the lattice mismatch  
 212 between MoSe<sub>2</sub> and PtSe<sub>2</sub>, the formation energy of an atomic  
 213 sharp interface should be very high. Figure 2e shows the initial  
 214 stage of the lateral boundary, displaying a sharp change from  
 215 PtSe<sub>2</sub> to MoSe<sub>2</sub> lattice with some tiny regions of bright  
 216 contrast along the edge. This indicates that both PtSe<sub>2</sub> and  
 217 MoSe<sub>2</sub> lattices have a sharp edge termination without any  
 218 chemical bonding. Figure 2f shows another region of the lateral  
 219 boundary away from Figure 2e, where the transition region  
 220 between the PtSe<sub>2</sub>/MoSe<sub>2</sub> Moiré pattern and bilayer MoSe<sub>2</sub>  
 221 shows an enhanced contrast. This is due to the overlap of the  
 222 edge regions from the two monolayers, that is, the PtSe<sub>2</sub> layer  
 223 has rolled on top of the bilayer MoSe<sub>2</sub> edge, forming a thicker  
 224 layer which exhibits brighter contrast, as illustrated by the  
 225 corresponding atomic model (Figure 2g,h). The overlapping  
 226 region varies and becomes wider (Figure 2d) along the  
 227 boundary, confirming the overlapping feature in the lateral  
 228 boundary. This is consistent with our expectation that the  
 229 PtSe<sub>2</sub> is more likely to climb over the MoSe<sub>2</sub> edge (second  
 230 layer MoSe<sub>2</sub>) during the growth to form a vertically  
 231 overlapping boundary since the formation energy of an  
 232 interconnected in-plane boundary is very high, due to their  
 233 lattice mismatch.

It is known that the interlayer interaction offers great  
 opportunity to study different properties in van der Waals  
 (vdW) solids, for instance, the electronic structure from the  
 Moiré pattern in a vdW heterostructure.<sup>27–29</sup> Substantial  
 research efforts have been devoted to weak interlayer coupled  
 TMDs and their heterostructures, for example, MoSe<sub>2</sub> and  
 WSe<sub>2</sub>.<sup>27</sup> Strong interlayer coupled two-dimensional (2D)  
 materials have recently been visited,<sup>2,5,30,31</sup> and PtSe<sub>2</sub> is a  
 representative among them. An interesting question then arises  
 regarding the interlayer coupling of a heterostructure whose  
 components provide strong and weak interlayer couplings,  
 respectively. The PtSe<sub>2</sub>/MoSe<sub>2</sub> heterostructure synthesized in  
 this work offers an ideal platform for studying this special  
 interlayer interaction. The fully relaxed atomic structure of the  
 PtSe<sub>2</sub>(1T)/MoSe<sub>2</sub>(1H) vertical heterostructure is shown in  
 Figure 3. According to the STEM measured Moiré periodicity  
 (Figure 2), a 7 × 7 supercell of the PtSe<sub>2</sub> monolayer stacking  
 over an 8 × 8 supercell the MoSe<sub>2</sub> monolayer is adopted for  
 modeling the heterostructure. The optimized lattice constant  
 of the supercell is 2.64 nm, only 1.4% larger than the  
 experimental value of 2.60 nm. It is exceptional that MoSe<sub>2</sub>  
 appears rumpling in the relaxed heterojunction, suggesting  
 significant interlayer attraction (0.25 eV/PtSe<sub>2</sub>) between the  
 two layers and stronger bending strength of PtSe<sub>2</sub> than that of  
 MoSe<sub>2</sub>. The interlayer distance *d* varies from 3.15 to 3.64 Å,  
 whose lower limit is much larger than that of PtSe<sub>2</sub> bilayers of  
 2.55 Å<sup>5</sup> but slightly smaller than that of MoSe<sub>2</sub> bilayers of 3.20  
 Å,<sup>32</sup> implying the interlayer interaction might be stronger than

262 that in MoSe<sub>2</sub>. The mismatched lattices of 1L PtSe<sub>2</sub> (3.71 Å for  
263 theory and 3.76 Å for experiment) and 1L MoSe<sub>2</sub> (3.30 Å for  
264 theory and 3.32 Å for experiment) lead to continuously varied  
265 stacking orders. There are seven local stacking orders along the  
266 supercell lattice. Among them, we found three high-symmetry  
267 ones, namely Se<sub>inter-PtSe<sub>2</sub></sub> on top of Se<sub>inter-MoSe<sub>2</sub></sub> (Figure 3c,  
268 denoted by the violet rectangle), Pt on top of Se<sub>inter-MoSe<sub>2</sub></sub>  
269 (Figure 3d, denoted by the green rectangle), and Se<sub>inter-PtSe<sub>2</sub></sub>  
270 on top of Mo (Figure 3e, denoted by the red rectangle). The  
271 vertical distances of these three stacking orders are 3.64, 3.17,  
272 and 3.15 Å, respectively (Figure S15a). Correspondingly, the  
273 spatial modulations of local bandgap and valence band  
274 maximum (VBM) of this vertical heterostructure are shown  
275 in Figures S15b, S16, and S17, respectively, where the  
276 variations of bandgaps and VBMs share the same modulation  
277 pattern with that of vertical interlayer distances. The Moiré  
278 potential (VBM) for the above three high-symmetry stacking  
279 orders are -65, -5, and 0 meV, respectively.

280 Atom-decomposed band structures (Figure 4a) explicitly  
281 show seven emerging states (denoted bands 1–7) in addition  
282 to a type II band alignment of the heterojunctions. The valence  
283 and conduction bands are comprised of the VB of MoSe<sub>2</sub> (Mo-  
284 d orbital, Se-p orbital) and CB of PtSe<sub>2</sub> (Pt-d orbital, Se-p  
285 orbital), respectively (Figure 4b,c). Figure 4d illustrates the  
286 band alignment before and after forming the heterojunction.  
287 The junction has a direct bandgap of 0.94 eV (0.92 eV, w/  
288 SOC), reduced from a 1.51 eV (1.39 eV, w/SOC) direct  
289 bandgap of MoSe<sub>2</sub> and a 1.34 eV (1.19 eV, w/SOC) indirect  
290 bandgap of PtSe<sub>2</sub>, which are in good accordance with their  
291 experimental values, that is, 1.55 eV for MoSe<sub>2</sub><sup>33</sup> and 1.13 eV  
292 for PtSe<sub>2</sub>.<sup>5</sup> These seven bands are not induced by the  
293 aforementioned substantial structural deformation of MoSe<sub>2</sub>  
294 or PtSe<sub>2</sub>, as Figure 4b,c shows that the deformation does not  
295 change the shape of band structures. They are also not the case  
296 of quantum confined states<sup>29</sup> since both MoSe<sub>2</sub> and PtSe<sub>2</sub>  
297 contribute to them. Bands 1–7 are thus regarded as  
298 electronically hybridized interfacial states, which result from  
299 the frustrated strong-weak interlayer coupling between PtSe<sub>2</sub>  
300 and MoSe<sub>2</sub> layers. These hybridized interfacial states, emerging  
301 within the original bandgap of vdW heterojunctions, are of  
302 particular interest. Figure 4e–g plots the spatial distributions of  
303 the wave function norms of bands 1 (e), 4 (f) and 7 (g). They  
304 are located around the aforementioned three particular  
305 stacking positions as marked by red, green, and violet  
306 rectangles, respectively, indicating each interfacial state  
307 corresponds to one stacking configuration. The side views  
308 (Figure 4e–g) suggest that these interfacial states are  
309 comprised of p<sub>z</sub> orbitals of the interfacial Se layer of MoSe<sub>2</sub>  
310 and both Se layers of PtSe<sub>2</sub> and d<sub>z<sup>2</sup></sub> orbital of Pt and Mo atoms,  
311 implying that the outer Se layer of MoSe<sub>2</sub> is not involved in  
312 forming these interfacial states. These wave functions are more  
313 localized than those of VB and CB (Figure S18) in real-space,  
314 consistent with the flat band dispersion in the *k*-space. These  
315 spatially localized bands suggest that electron–hole pairs of a  
316 given energy are excited at a certain stacking position, as  
317 marked in Figure 3a. The PtSe<sub>2</sub> involved in forming these  
318 bands may lead to inter- and intralayer mixed excitation  
319 mechanisms for the interlayer excitons, which should be  
320 interesting for further exploration. In the light of these,  
321 interfacial states are of particular interest in terms of exciton  
322 dynamics in the heterojunction.

As discussed above, STEM images and first-principles  
calculations have demonstrated the vertical stacking and  
emerging interfacial states in PtSe<sub>2</sub>/MoSe<sub>2</sub> heterostructure  
due to the frustrated strong–weak interlayer coupling between  
PtSe<sub>2</sub> and MoSe<sub>2</sub> layers. In order to further elucidate the  
interfacial states and the interlayer coupling, we conducted the  
electrostatic force microscopy (EFM) to study the charge  
distribution in PtSe<sub>2</sub>/MoSe<sub>2</sub> heterostructures. EFM has been  
proven as an effective method to evaluate the local electrical  
properties of 2D materials.<sup>34,35</sup> The optical image and  
topography of PtSe<sub>2</sub>/MoSe<sub>2</sub> heterostructure are shown in  
Figure 5a,c, respectively. The corresponding AFM image is

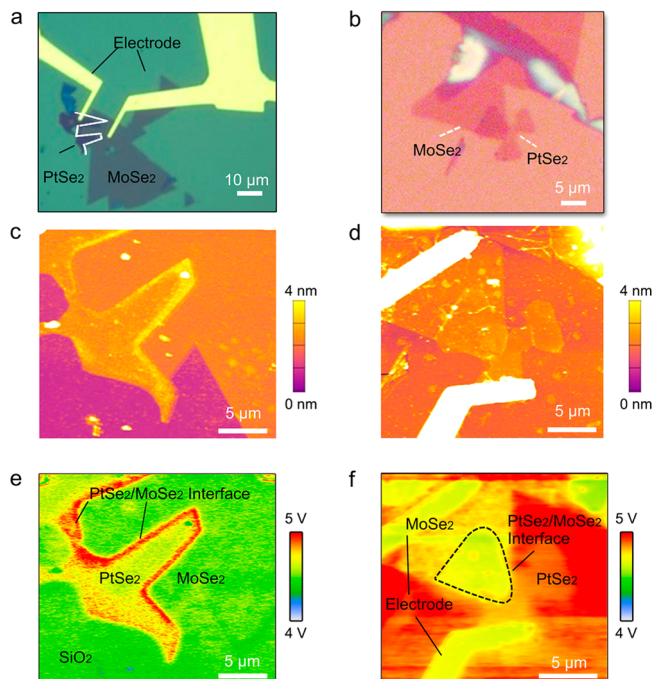


**Figure 5.** EFM measurements. (a and c) Optical image and height topography of PtSe<sub>2</sub>/MoSe<sub>2</sub> heterostructure grown by one-step CVD. (b and d) Optical image and topography of transferred PtSe<sub>2</sub>/MoSe<sub>2</sub> heterostructure. (e) EFM image of PtSe<sub>2</sub>/MoSe<sub>2</sub>, identifying the edge state at the edge of PtSe<sub>2</sub>. (f) EFM image of transferred PtSe<sub>2</sub>/MoSe<sub>2</sub> under zero bias voltage, indicating a semiconducting behavior of PtSe<sub>2</sub> and MoSe<sub>2</sub>.

presented in Figure S19. The EFM image of the hetero-  
structure shown in Figure 5e indicates that strong charge  
accumulation takes place on the edge of PtSe<sub>2</sub>, which is  
attributed to the charge transfer from uncovered monolayer  
MoSe<sub>2</sub> to PtSe<sub>2</sub>/MoSe<sub>2</sub> heterostructure induced by the slightly  
lowered VB of PtSe<sub>2</sub> and lifted CB of MoSe<sub>2</sub>. For comparison,  
EFM measurement was carried out on a transferred PtSe<sub>2</sub>/  
MoSe<sub>2</sub> heterostructure. The optical image, topography, and  
EFM image are shown in Figure 5b,d,f, respectively. The  
absence of edge states clearly illustrates that the strong  
interlayer coupling is not formed in the transferred  
heterostructure. These results demonstrate the strong inter-  
layer coupling between strong interlayer-coupled PtSe<sub>2</sub> and  
weak interlayer-coupled MoSe<sub>2</sub>, which agrees well with the  
results of electronically hybridized interface states from first-  
principles calculations.

The type II band alignment offers the possibility to study the  
charge transfer induced by the interlayer coupling in PtSe<sub>2</sub>/  
MoSe<sub>2</sub>

353 MoSe<sub>2</sub> heterostructure. We further studied the charge transfer  
 354 kinetics of PtSe<sub>2</sub>/MoSe<sub>2</sub> heterostructure through ultrafast  
 355 transient dynamics measurement. The ultrafast transient  
 356 reflection dynamics of the heterostructure along with the  
 357 PtSe<sub>2</sub> and MoSe<sub>2</sub> monolayers (optical images are shown as  
 358 insets in Figure 6a,b) were measured using 910 nm pump

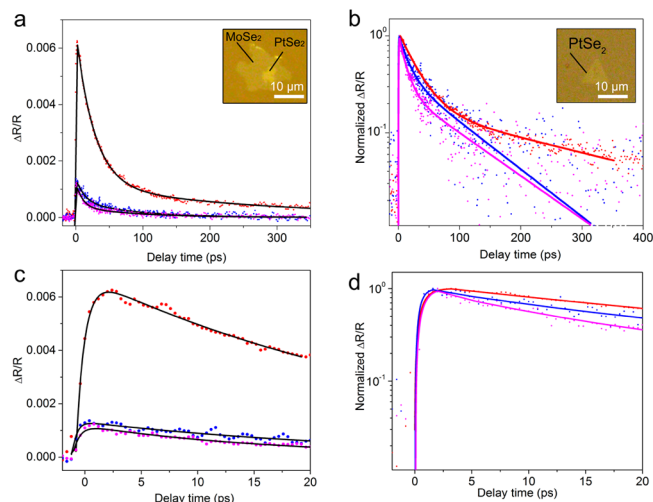


**Figure 6.** Ultrafast electron dynamics of MoSe<sub>2</sub>, PtSe<sub>2</sub>, and PtSe<sub>2</sub>/MoSe<sub>2</sub> heterostructure. (a) Differential reflection kinetics of PtSe<sub>2</sub>/MoSe<sub>2</sub> heterostructure (red), PtSe<sub>2</sub> (blue), and MoSe<sub>2</sub> (pink) monolayers excited at 910 nm and probed at 780 nm with the pump and probe power around 100 and 70  $\mu$ W, respectively. Insets is the optical image of PtSe<sub>2</sub>/MoSe<sub>2</sub> heterostructure. The kinetics at shorter time scale is shown in (c). (b) Comparison of the normalized differential reflection kinetics of the heterostructure and monolayers. Inset is the optical image of PtSe<sub>2</sub>. The corresponding kinetics at shorter time scale of PtSe<sub>2</sub> is displayed in (d).

359 excitation and 780 nm probe with pump and probe powers of  
 360 100 and 70  $\mu$ W, respectively. According to the reported  
 361 experimental band gaps of monolayer MoSe<sub>2</sub> (1.55 eV)<sup>33</sup> and  
 362 PtSe<sub>2</sub> (1.13 eV)<sup>5</sup> as well as our band calculation results, the  
 363 910 nm pump excitation will only excite carriers in PtSe<sub>2</sub>, since  
 364 the photon energy is below the bandgap of MoSe<sub>2</sub>. Thus,  
 365 direct one-photon absorption of 910 nm wavelength will not  
 366 occur in MoSe<sub>2</sub> layers. As shown in Figure 6, the transient  
 367 response from the heterostructure is very different from that of  
 368 monolayers under the same pump–probe power. First, the  
 369 transient response amplitude of the heterostructure is  $\sim$ 3 times  
 370 higher than that of individual monolayers (Figure 6a). Second,  
 371 the initial rising time of the transient response is slightly slower  
 372 in heterostructure than that in individual monolayers. Third,  
 373 the subsequent decay dynamics are relatively longer for  
 374 heterostructure than either PtSe<sub>2</sub> or MoSe<sub>2</sub> monolayer alone.  
 375 The latter two features can be clearly visualized from the  
 376 normalized transient reflection kinetics shown in Figure 6b.

377 Compared with monolayer PtSe<sub>2</sub>, the relatively slow rising  
 378 kinetics of the PtSe<sub>2</sub>/MoSe<sub>2</sub> heterostructure proves the hole  
 379 transfer between PtSe<sub>2</sub> and MoSe<sub>2</sub>. More specifically, the pump  
 380 (910 nm) excites electrons from the VB to the CB of PtSe<sub>2</sub>  
 381 through one photon absorption, along with a rapid hole  
 382 transfer from PtSe<sub>2</sub> to MoSe<sub>2</sub> layer due to their type II band  
 383 alignment. The rising time ( $\tau_r$ ) of the heterostructure kinetics,  
 384 which describes the hole transfer between PtSe<sub>2</sub> and MoSe<sub>2</sub>, is  
 385 found to be 0.5–0.9 ps. This value is longer than that of PtSe<sub>2</sub>

monolayers and consistent with the previous reports on the  
 charge-transfer process in heterostructures.<sup>36</sup> As a result of the  
 hole transfer from PtSe<sub>2</sub> to MoSe<sub>2</sub>, the probe reflection is  
 modified due to the hole occupation in MoSe<sub>2</sub> and contributes  
 to transient reflection signal of the 780 nm probe. The  
 magnitude of peak transient signal is also 5 times larger than  
 that in individual PtSe<sub>2</sub> or MoSe<sub>2</sub> monolayers.

The following decay kinetics after the maximum transient  
 reflection of the heterostructure and monolayers can be fitted  
 with biexponential function  $I(t) = A \times \exp(-t/\tau_{d1}) + B \times$   
 $\exp(-t/\tau_{d2})$ , where  $\tau_{d1}$  and  $\tau_{d2}$  represent the fast and slow  
 decay time constants, respectively. The fast ( $\tau_{d1} = 27.5 \pm 0.3$   
 ps) and slow ( $\tau_{d2} = 280.1 \pm 12.3$  ps) decay time constants of  
 the heterostructure are nearly 2–3 times larger than decay time  
 constants of individual PtSe<sub>2</sub> ( $\tau_{d1} = 14.9 \pm 1.8$  ps,  $\tau_{d2} = 88.8 \pm$   
 9 ps) and MoSe<sub>2</sub> ( $\tau_{d1} = 11.7 \pm 0.9$  ps,  $\tau_{d2} = 97.9 \pm 9$  ps)  
 monolayers. The decay time of PtSe<sub>2</sub>/MoSe<sub>2</sub> heterostructure is  
 much longer than that of PtSe<sub>2</sub> and MoSe<sub>2</sub> monolayers, which  
 suggests an efficient separation of the electron–hole in PtSe<sub>2</sub>/  
 MoSe<sub>2</sub> heterostructures.

## CONCLUSIONS

In summary, we have successfully synthesized PtSe<sub>2</sub>/MoSe<sub>2</sub>  
 vertically stacked heterojunctions *via* a one-step CVD method.  
 STEM results confirm the formation of vertical and lateral  
 heterostructures between strong interlayer-coupled PtSe<sub>2</sub> and  
 weak interlayer-coupled MoSe<sub>2</sub>. First-principle calculations  
 confirm a direct band gap structure and type II band alignment  
 between PtSe<sub>2</sub> and MoSe<sub>2</sub>. The emerging electronically  
 hybridized interface states within the original bandgap are  
 observed in CVD-grown 2D TMD heterostructures, which  
 have been confirmed by the edge states unveiled by EFM.  
 Ultrafast electron dynamics measurements suggest that the  
 holes transfer from MoSe<sub>2</sub> to PtSe<sub>2</sub>, confirming the  
 theoretically predicted band alignment and strong interlayer  
 coupling between PtSe<sub>2</sub> and MoSe<sub>2</sub>. This strategy shows the  
 way toward the synthesis of heterostructures based on group  
 10 TMDs, and our results show great potential of PtSe<sub>2</sub>/  
 MoSe<sub>2</sub> heterostructures for applications in electronic and  
 optoelectronic devices.

## METHODS

**PtSe<sub>2</sub> and PtSe<sub>2</sub>/MoSe<sub>2</sub> Growth.** In our experiment, PtCl<sub>2</sub>,  
 MoO<sub>3</sub>, and Se were used as sources (all reactants were bought from  
 Alfa Aesar with purity more than 99%). The polycrystalline PtSe<sub>2</sub> film  
 was grown in a quartz tube (1 in. diameter, 36 cm length) at 400  $^{\circ}$ C.  
 Single PtSe<sub>2</sub> and PtSe<sub>2</sub>/MoSe<sub>2</sub> flakes were synthesized using the same  
 setup at 810  $^{\circ}$ C. The distance between PtCl<sub>2</sub> and mixed powder is  $\sim$ 5  
 mm. H<sub>2</sub>/Ar was used as the carrier gas. Specifically, the alumina boat  
 (8 cm  $\times$  1.1 cm  $\times$  1.2 cm) containing Mo and Pt precursors was put  
 in the middle of the quartz tube. The distance between the precursors  
 and substrate is around 1.2 cm. For PtSe<sub>2</sub>, Ar (or Ar/H<sub>2</sub> mix) gas with  
 a flow rate of 80 (80/10) sccm was used as the carrier gas, and the  
 Al<sub>2</sub>O<sub>3</sub> boat containing 10 mg PtCl<sub>2</sub> was put in the center of the tube.  
 The SiO<sub>2</sub>/Si substrate was placed on the boat with surface downside.  
 Another Al<sub>2</sub>O<sub>3</sub> boat containing 100 mg Se powder was put in the  
 upstream zone. The temperature was ramped up to 810  $^{\circ}$ C in 16 min  
 and kept at the reaction temperature for 15 min. Then the furnace was  
 cooled down to room temperature naturally.

For PtSe<sub>2</sub>/MoSe<sub>2</sub>, the Ar/H<sub>2</sub> mixed gas with a flow rate of 80/10  
 sccm was used as the carrier gas, and the Al<sub>2</sub>O<sub>3</sub> boat containing 5 mg  
 PtCl<sub>2</sub> and 5 mg (4 mg MoO<sub>3</sub> and 1 mg NaCl) was put in the center of  
 the tube. The distance between PtCl<sub>2</sub> and MoO<sub>3</sub>/NaCl was 5 mm.  
 SiO<sub>2</sub>/Si or sapphire substrate was placed on the boat with surface  
 downside. Another Al<sub>2</sub>O<sub>3</sub> boat containing 10 g Se powder was put on

449 the upstream zone. The temperature was ramped up to 810 °C in 16  
450 min and kept at the reaction temperature for 10 min. The furnace was  
451 then cooled down to room temperature gradually.

452 For PtSe<sub>2</sub>/MoSe<sub>2</sub> heterostructure prepared by mechanic exfoliation  
453 and transfer, a 0.8 μm layer of poly(methyl methacrylate) (PMMA)  
454 was spin-coated on the MoSe<sub>2</sub> wafer and then baked at 180 °C for 4  
455 min. Afterward, the wafer was immersed in KOH solution (1M) to  
456 etch the SiO<sub>2</sub> layer. After lift-off, the PMMA/PtSe<sub>2</sub>/MoSe<sub>2</sub> film was  
457 transferred into DI water for several cycles to wash away the residual  
458 contaminants and then dried in air. Next, PMMA with MoSe<sub>2</sub> samples  
459 were transferred on PtSe<sub>2</sub> flakes. Last, the wafer was immersed in  
460 acetone solution to resolve the PMMA.

461 **Raman Characterization.** Raman measurements with an  
462 excitation laser of 532 nm were performed using WITEC alpha  
463 300R Confocal Raman system. Before Raman characterization, the  
464 system was calibrated with the Raman peak of Si at 520 cm<sup>-1</sup>. The  
465 laser powers were set at <1 mW to avoid overheat the samples.

466 **AFM.** AFM measurement was carried out using the Asylum  
467 Research, Cypher S system with a cantilever tip of Arrow-NCR-50-  
468 Silicon SPM-Sensor (coating on detector sider: Al-coating). The force  
469 constant is 42 N/m.

470 **XPS Characterization.** XPS measurement was performed using a  
471 monochromated Al Kα source ( $h\nu = 1486.6$  eV) and a 128 channel  
472 mode detection PHI original detector. XPS spectra were acquired at a  
473 pass energy of 140 eV and takeoff angle of 45°.

474 **TEM and STEM Characterization.** The STEM samples were  
475 prepared with a PMMA assisted method. A layer of PMMA about 0.8  
476 μm in thickness was spin-coated on the wafer with samples deposited  
477 and then baked at 140 °C for 5 min. Afterward, the wafer was  
478 immersed in KOH solution (1 M) to etch the SiO<sub>2</sub> layer overnight.  
479 After lift-off, the PMMA/PtSe<sub>2</sub>/MoSe<sub>2</sub> film was transferred into DI  
480 water for several cycles to wash away the residual contaminants and  
481 then fished by a TEM grid (Quantifoil Mo grid). The transferred  
482 specimen was dried naturally in ambient environment and then  
483 dropped into acetone overnight to wash away the PMMA coating  
484 layers. The STEM imaging was done in a JEOL 2100F with delta  
485 probe corrector, which corrects the aberration up to fifth order,  
486 resulting in a probe size of 1.2 Å. The imaging was conducted at an  
487 acceleration voltage of 60 kV. The convergent angle for illumination is  
488 about 35 mrad, with a collection detector angle ranging from 45 to  
489 200 mrad. The BF-TEM and diffraction imaging was conducted in a  
490 FEI Tecnai F30 microscope operating at 80 kV. All imaging was  
491 performed at room temperature.

492 **Ultrafast Transient Reflection Spectroscopy.** An infrared  
493 optical parametric amplifier (OPA) pumped by a 60 fs, 250 kHz  
494 Ti:Sapphire regenerative amplifier (RegA) was used in the transient  
495 reflection measurements. The idler from OPA at 1840 nm used as  
496 pump is frequency doubled to 920 nm (~180 fs). The 780 nm  
497 component filtered from white light supercontinuum, which is  
498 generated from a sapphire crystal pumped with compressed remnant  
499 800 nm beam of OPA, was used as a probe. Both pump and probe  
500 pulses were linearly polarized. A 40× reflective objective lens was used  
501 to focus the co-propagating pump probe spots onto the sample. The  
502 reflected probe was collected by the same objective lens and routed  
503 through a monochromator followed by a photodetector. The detected  
504 probe reflection was read by a lock-in amplifier referenced to a  
505 mechanically chopped pump. The probe spot size was estimated to be  
506 2 μm. The pump photon fluency was estimated to be around  $1 \times 10^{16}$   
507 photons/cm<sup>2</sup>.

508 **Calculations.** Density functional theory (DFT) calculations were  
509 performed using the generalized gradient approximation for the  
510 exchange–correlation potential, the projector augmented wave  
511 method,<sup>37,38</sup> and a plane-wave basis set as implemented in the  
512 Vienna *ab initio* simulation package (VASP).<sup>39</sup> For the configuration  
513 of PtSe<sub>2</sub>(1T)/MoSe<sub>2</sub>(1H) vertical heterostructure, a (7 × 7) supercell  
514 is adopted for PtSe<sub>2</sub>(1T), while a (8 × 8) supercell for MoSe<sub>2</sub>(1H)  
515 and a vacuum layer of 25 Å in thickness between periodic images was  
516 employed. The energy cutoff for the plane-wave basis was set to 500  
517 eV for all calculations except those with spin–orbit coupling (SOC)  
518 into consideration where an energy cutoff of 300 eV is utilized. The

inclusion of SOC has little influence on the shape of the band  
519 structures but induces appreciable band energy shifts or band  
520 splitting, for example, a separation of 30–50 meV for the emerging  
521 hybridized interfacial states marked with bands 1–7 in Figure 4a. All  
522 calculations and analysis shown in Figure 4a–c were performed in the  
523 same supercell which consisted of a (7 × 7) supercell of PtSe<sub>2</sub>(1T)  
524 and a (8 × 8) supercell of MoSe<sub>2</sub>(1H). In optimizing the system  
525 geometry, vdW interactions were considered at the vdW-DF<sup>40</sup> level  
526 with the optB86b (optB86b-vdW) functional for exchange potential,<sup>41</sup>  
527 which was recently demonstrated more accurate in describing  
528 structural properties of layered materials than other functionals.<sup>31,42,43</sup>  
529 All atoms in the supercell were allowed to relax until the residual force  
530 per atom was <0.02 eV·Å<sup>-1</sup>.  
531

## ASSOCIATED CONTENT

### Supporting Information

The Supporting Information is available free of charge on the  
ACS Publications website at DOI: 10.1021/acsnano.8b09479.

Further experimental and theoretical details, including  
different size of vertical heterostructures, thickness and  
Raman spectrum of PtSe<sub>2</sub>, optical images of PtSe<sub>2</sub>/  
MoSe<sub>2</sub> heterostructure, growth of PtSe<sub>2</sub> on exfoliated  
MoSe<sub>2</sub> flakes, optical image and TEM characterization of  
polycrystalline PtSe<sub>2</sub>, optical images, AFM images and  
Raman spectra of PtSe<sub>2</sub> single crystals, optical images  
and AFM images of PtSe<sub>2</sub> single crystals synthesized on  
sapphire substrate, XPS characterizations of PtSe<sub>2</sub>/  
MoSe<sub>2</sub> heterostructure, PL spectra, PL and Raman  
mappings of PtSe<sub>2</sub>/MoSe<sub>2</sub> with different shape, SEAD  
patterns of PtSe<sub>2</sub>/MoSe<sub>2</sub> heterostructure, large-scale  
STEM image of vertically stacked PtSe<sub>2</sub>/MoSe<sub>2</sub>  
heterostructure, optical image of in plane and vertical  
PtSe<sub>2</sub>/MoSe<sub>2</sub> heterostructures, spatial distribution of  
interlayer distance and bandgap for PtSe<sub>2</sub>(1T)/  
MoSe<sub>2</sub>(1H) vertical heterostructure, spatial distribution  
of bandgap for PtSe<sub>2</sub>(1T)/MoSe<sub>2</sub>(1H) vertical hetero-  
structure, spatial distribution of VBM for PtSe<sub>2</sub>(1T)/  
MoSe<sub>2</sub>(1H) vertical heterostructure, spatial structures of  
wave functions for PtSe<sub>2</sub>(1T)/MoSe<sub>2</sub>(1H) vertical  
heterostructures, AFM image and thickness of PtSe<sub>2</sub>  
on MoSe<sub>2</sub> (PDF)

## AUTHOR INFORMATION

### Corresponding Authors

\*E-mail: z.liu@ntu.edu.sg.

\*E-mail: wji@ruc.edu.cn.

\*E-mail: sundong@pku.edu.cn.

\*E-mail: lin.junhao.stem@gmail.com.

### ORCID

Xianghua Kong: 0000-0003-4381-4955

Zhihai Cheng: 0000-0003-4938-4490

Ting Yu: 0000-0001-5782-1588

Kazu Suenaga: 0000-0002-6107-1123

Dong Sun: 0000-0002-0898-4548

Wei Ji: 0000-0001-5249-6624

Zheng Liu: 0000-0002-8825-7198

### Author Contributions

•These authors contributed equally to this work.

### Notes

The authors declare no competing financial interest.

## 577 ACKNOWLEDGMENTS

578 This work is supported by the Singapore National Research  
579 Foundation under NRF RF award no. NRF-RF2013-08. MOE  
580 Tier 1 RG7/18, MOE Tier 2 MOE2015-T2-2-007, MOE2016-  
581 T2-2-153, MOE2017-T2-2-136, MOE Tier 3 MOE2018-T3-1-  
582 002, and A\*Star QTE program. J.L. and K.S. acknowledge JST-  
583 ACCEL and JSPS KAKENHI (JP16H06333 and P16823) for  
584 financial support. This work was also supported by the Pico  
585 Center at MCPC of SUSTech that receives support from  
586 Presidential fund and Development and Reform Commission  
587 of Shenzhen Municipality. Z.-H.L. thanks the A\*STAR Science  
588 and Engineering Research Council (122 360 0008) and the  
589 Ministry of Education (MOE2014-T2-2-052) for financial  
590 support. Z.H.C. thanks the Ministry of Science and  
591 Technology (MOST) of China (no. 2016YFA0200700) for  
592 financial support. X.K. Z.H.C., R.X., and W.J. were supported  
593 by the National Natural Science Foundation of China (grant  
594 nos. 11274380, 91433103, 11622437, 21622304, 61674045,  
595 11604063, and 61674171), the Fundamental Research Funds  
596 for the Central Universities of China and the Research Funds  
597 of Renmin University of China (grant nos. 16XNLQ01 and  
598 18XNLG01), and the Strategic Priority Research Program of  
599 Chinese Academy of Sciences (grant no. XDB30000000). This  
600 research is partially supported by the Science, Technology, and  
601 Innovation Commission of Shenzhen Municipality (no.  
602 ZDSYS20170303165926217). X.K. thanks Prof. Hong Guo  
603 at McGill University for financial support. C.M., W.L., and D.S.  
604 were supported by the National Natural Science Foundation of  
605 China (grant nos. 11674013, 11704012). Calculations were  
606 performed at the physics lab of high-performance computing of  
607 Renmin University of China, Shanghai Supercomputer Center,  
608 McGill University, Calcul Québec, and Compute Canada.

## 609 REFERENCES

610 (1) Yao, W.; Wang, E. Y.; Huang, H. Q.; Deng, K.; Yan, M. Z.;  
611 Zhang, K. N.; Miyamoto, K.; Okuda, T.; Li, L. F.; Wang, Y. L.; Gao,  
612 H. J.; Liu, C. X.; Duan, W. H.; Zhou, S. Y. Direct Observation of Spin-  
613 Layer Locking by Local Rashba Effect in Monolayer Semiconducting  
614 PtSe<sub>2</sub> Film. *Nat. Commun.* **2017**, *8*, 142216.  
615 (2) Zhao, Y. D.; Qiao, J. S.; Yu, P.; Hu, Z. X.; Lin, Z. Y.; Lau, S. P.;  
616 Liu, Z.; Ji, W.; Chai, Y. Extraordinarily Strong Interlayer Interaction in  
617 2D Layered PtS<sub>2</sub>. *Adv. Mater.* **2016**, *28*, 2399–2407.  
618 (3) Ciarrocchi, A.; Avsar, A.; Ovchinnikov, D.; Kis, A. Thickness-  
619 Modulated Metal-to-Semiconductor Transformation in a Transition  
620 Metal Dichalcogenide. *Nat. Commun.* **2018**, *9*, 919.  
621 (4) Li, P. F.; Li, L.; Zeng, X. C. Tuning the Electronic Properties of  
622 Monolayer and Bilayer PtSe<sub>2</sub> via Strain Engineering. *J. Mater. Chem. C*  
623 **2016**, *4*, 3106–3112.  
624 (5) Zhao, Y. D.; Qiao, J. S.; Yu, Z. H.; Yu, P.; Xu, K.; Lau, S. P.;  
625 Zhou, W.; Liu, Z.; Wang, X. R.; Ji, W.; Chai, Y. High-Electron-  
626 Mobility and Air-Stable 2D Layered PtSe<sub>2</sub> FETs. *Adv. Mater.* **2017**,  
627 *29*, 1604230.  
628 (6) Zeng, L.; Lin, S.; Lou, Z.; Yuan, H.; Long, H.; Li, Y.; Lu, W.;  
629 Lau, S. P.; Wu, D.; Tsang, Y. H. Ultrafast and Sensitive Photodetector  
630 Based on a PtSe<sub>2</sub>/Silicon Nanowire Array Heterojunction with a  
631 Multiband Spectral Response from 200 to 1550 nm. *NPG Asia Mater.*  
632 **2018**, *10*, 352–362.  
633 (7) Yu, X. C.; Yu, P.; Wu, D.; Singh, B.; Zeng, Q. S.; Lin, H.; Zhou,  
634 W.; Lin, J. H.; Suenaga, K.; Liu, Z.; Wang, Q. J. Atomically Thin  
635 Noble Metal Dichalcogenide: A Broadband Mid-Infrared Semi-  
636 conductor. *Nat. Commun.* **2018**, *9*, 1545.  
637 (8) Chia, X. Y.; Adriano, A.; Lazar, P.; Sofer, Z.; Luxa, J.; Pumera, M.  
638 Layered Platinum Dichalcogenides (PtS<sub>2</sub>, PtSe<sub>2</sub>, and PtTe<sub>2</sub>) Electro-  
639 catalysis: Monotonic Dependence on the Chalcogen Size. *Adv. Funct.*  
640 *Mater.* **2016**, *26*, 4306–4318.

(9) Yim, C.; Lee, K.; McEvoy, N.; O'Brien, M.; Riazimehr, S.; 641  
Bernier, N. C.; Cullen, C. P.; Kotakoski, J.; Meyer, J. C.; Lemme, M. 642  
C.; Duesberg, G. S. High-Performance Hybrid Electronic Devices 643  
from Layered PtSe<sub>2</sub> Films Grown at Low Temperature. *ACS Nano* 644  
**2016**, *10*, 9550–9558. 645  
(10) Liu, K.; Zheng, B. J.; Wu, J. J.; Chen, Y. F.; Wang, X. Q.; Qi, F.; 646  
He, D. W.; Zhang, W. L.; Li, Y. R. Synthesis of Two-Dimensional 647  
Semiconductor Single-Crystal PtSe<sub>2</sub> under High Pressure. *J. Mater.* 648  
*Sci.* **2018**, *53*, 1256–1263. 649  
(11) Yan, M. Z.; Wang, E. Y.; Zhou, X.; Zhang, G. Q.; Zhang, H. Y.; 650  
Zhang, K. N.; Yao, W.; Lu, N. P.; Yang, S. Z.; Wu, S. L.; Yoshikawa, 651  
T.; Miyamoto, K.; Okuda, T.; Wu, Y.; Yu, P.; Duan, W. H.; Zhou, S. 652  
Y. High Quality Atomically Thin PtSe<sub>2</sub> Films Grown by Molecular 653  
Beam Epitaxy. *2D Mater.* **2017**, *4*, 045015. 654  
(12) Wang, Y. L.; Li, L. F.; Yao, W.; Song, S. R.; Sun, J. T.; Pan, J. B.; 655  
Ren, X.; Li, C.; Okunishi, E.; Wang, Y. Q.; Wang, E. Y.; Shao, Y.; 656  
Zhang, Y. Y.; Yang, H. T.; Schwier, E. F.; Iwasawa, H.; Shimada, K.; 657  
Taniguchi, M.; Cheng, Z. H.; Zhou, S. Y.; et al. Monolayer PtSe<sub>2</sub>, a 658  
New Semiconducting Transition-Metal-Dichalcogenide, Epitaxially 659  
Grown by Direct Selenization of Pt. *Nano Lett.* **2015**, *15*, 4013–4018. 660  
(13) Wang, Z. G.; Li, Q.; Besenbacher, F.; Dong, M. D. Facile 661  
Synthesis of Single Crystal PtSe<sub>2</sub> Nanosheets for Nanoscale 662  
Electronics. *Adv. Mater.* **2016**, *28*, 10224–10229. 663  
(14) Zhou, J. D.; Lin, J. H.; Huang, X. W.; Zhou, Y.; Chen, Y.; Xia, 664  
J.; Wang, H.; Xie, Y.; Yu, H. M.; Lei, J. C.; Wu, D.; Liu, F. C.; Fu, Q. 665  
D.; Zeng, Q. S.; Hsu, C. H.; Yang, C. L.; Lu, L.; Yu, T.; Shen, Z. X.; 666  
Lin, H.; et al. A Library of Atomically Thin Metal Chalcogenides. 667  
*Nature* **2018**, *556*, 355–359. 668  
(15) Li, M. Y.; Shi, Y. M.; Cheng, C. C.; Lu, L. S.; Lin, Y. C.; Tang, 669  
H. L.; Tsai, M. L.; Chu, C. W.; Wei, K. H.; He, J. H.; Chang, W. H.; 670  
Suenaga, K.; Li, L. J. Epitaxial Growth of a Monolayer WSe<sub>2</sub>-MoS<sub>2</sub> 671  
Lateral *p-n* Junction with an Atomically Sharp Interface. *Science* **2015**, 672  
*349*, 524–528. 673  
(16) Chen, K.; Wan, X.; Wen, J. X.; Xie, W. G.; Kang, Z. W.; Zeng, 674  
X. L.; Chen, H. J.; Xu, J. B. Electronic Properties of MoS<sub>2</sub>-WS<sub>2</sub> 675  
Heterostructures Synthesized with Two-Step Lateral Epitaxial 676  
Strategy. *ACS Nano* **2015**, *9*, 9868–9876. 677  
(17) Chen, K.; Wan, X.; Xie, W. G.; Wen, J. X.; Kang, Z. W.; Zeng, 678  
X. L.; Chen, H. J.; Xu, J. B. Lateral Built-in Potential of Monolayer 679  
MoS<sub>2</sub>-WS<sub>2</sub> in-Plane Heterostructures by a Shortcut Growth Strategy. 680  
*Adv. Mater.* **2015**, *27*, 6431–6437. 681  
(18) Li, X. F.; Lin, M. W.; Lin, J. H.; Huang, B.; Puzosky, A. A.; Ma, 682  
C.; Wang, K.; Zhou, W.; Pantelides, S. T.; Chi, M. F.; Kravchenko, I.; 683  
Fowlkes, J.; Rouleau, C. M.; Geohegan, D. B.; Xiao, K. Two- 684  
Dimensional GaSe/MoSe<sub>2</sub> Misfit Bilayer Heterojunctions by Van Der 685  
Waals Epitaxy. *Sci. Adv.* **2016**, *2*, No. e1501882. 686  
(19) Yoo, Y. D.; Degregorio, Z. P.; Johns, J. E. Seed Crystal 687  
Homogeneity Controls Lateral and Vertical Heteroepitaxy of 688  
Monolayer MoS<sub>2</sub> and WS<sub>2</sub>. *J. Am. Chem. Soc.* **2015**, *137*, 14281– 689  
14287. 690  
(20) Zhang, T.; Jiang, B.; Xu, Z.; Mendes, R. G.; Xiao, Y.; Chen, L. 691  
F.; Fang, L. W.; Gemming, T.; Chen, S. L.; Rummeli, M. H.; Fu, L. 692  
Twinned Growth Behaviour of Two-Dimensional Materials. *Nat.* 693  
*Commun.* **2016**, *7*, 13911. 694  
(21) Gong, Y. J.; Lin, J. H.; Wang, X. L.; Shi, G.; Lei, S. D.; Lin, Z.; 695  
Zou, X. L.; Ye, G. L.; Vajtai, R.; Yakobson, B. I.; Terrones, H.; 696  
Terrones, M.; Tay, B. K.; Lou, J.; Pantelides, S. T.; Liu, Z.; Zhou, W.; 697  
Ajayan, P. M. Vertical and in-Plane Heterostructures from WS<sub>2</sub>/MoS<sub>2</sub> 698  
Monolayers. *Nat. Mater.* **2014**, *13*, 1135–1142. 699  
(22) Duan, X. D.; Wang, C.; Shaw, J. C.; Cheng, R.; Chen, Y.; Li, H. 700  
L.; Wu, X. P.; Tang, Y.; Zhang, Q. L.; Pan, A. L.; Jiang, J. H.; Yu, R. 701  
Q.; Huang, Y.; Duan, X. F. Lateral Epitaxial Growth of Two- 702  
Dimensional Layered Semiconductor Heterojunctions. *Nat. Nano-* 703  
*technol.* **2014**, *9*, 1024–1030. 704  
(23) Wang, X. L.; Gong, Y. J.; Shi, G.; Chow, W. L.; Keyshar, K.; Ye, 705  
G. L.; Vajtai, R.; Lou, J.; Liu, Z.; Ringe, E.; Tay, B. K.; Ajayan, P. M. 706  
Chemical Vapor Deposition Growth of Crystalline Monolayer MoSe<sub>2</sub>. 707  
*ACS Nano* **2014**, *8*, 5125–5131. 708

- 709 (24) O'Brien, M.; McEvoy, N.; Motta, C.; Zheng, J. Y.; Berner, N.  
710 C.; Kotakoski, J.; Elibol, K.; Pennycook, T. J.; Meyer, J. C.; Yim, C.;  
711 Abid, M.; Hallam, T.; Donegan, J. F.; Sanvito, S.; Duesberg, G. S.  
712 Raman Characterization of Platinum Diselenide Thin Films. *2D*  
713 *Mater.* **2016**, *3*, 021004.
- 714 (25) Kim, K.; Lee, J. U.; Nam, D.; Cheong, H. Davydov Splitting  
715 and Excitonic Resonance Effects in Raman Spectra of Few-Layer  
716 MoSe<sub>2</sub>. *ACS Nano* **2016**, *10*, 8113–20.
- 717 (26) Nam, D.; Lee, J. U.; Cheong, H. Excitation Energy Dependent  
718 Raman Spectrum of MoSe<sub>2</sub>. *Sci. Rep.* **2015**, *5*, 17113.
- 719 (27) Zhang, C. D.; Chuu, C. P.; Ren, X. B.; Li, M. Y.; Li, L. J.; Jin, C.  
720 H.; Chou, M. Y.; Shih, C. K. Interlayer Couplings, Moire Patterns,  
721 and 2D Electronic Superlattices in MoS<sub>2</sub>/WSe<sub>2</sub> Hetero-Bilayers. *Sci.*  
722 *Adv.* **2017**, *3*, No. e1601459.
- 723 (28) Hong, J. H.; Wang, C.; Liu, H. J.; Ren, X. B. A.; Chen, J. L.;  
724 Wang, G. Y.; Jia, J. F.; Xie, M. H.; Jin, C. H.; Ji, W.; Yuan, J.; Zhang, Z.  
725 Inversion Domain Boundary Induced Stacking and Bandstructure  
726 Diversity in Bilayer MoSe<sub>2</sub>. *Nano Lett.* **2017**, *17*, 6653–6660.
- 727 (29) Pan, Y.; Folsch, S.; Nie, Y. F.; Waters, D.; Lin, Y. C.; Jariwala,  
728 B.; Zhang, K. H.; Cho, K.; Robinson, J. A.; Feenstra, R. M. Quantum-  
729 Confined Electronic States Arising from the Moire Pattern of MoS<sub>2</sub>-  
730 WSe<sub>2</sub> Heterobilayers. *Nano Lett.* **2018**, *18*, 1849–1855.
- 731 (30) Qiao, J.; Pan, Y.; Yang, F.; Wang, C.; Chai, Y.; Ji, W. Few-Layer  
732 Tellurium: One-Dimensional-Like Layered Elementary Semiconduc-  
733 tor with Striking Physical Properties. *Sci. Bull.* **2018**, *63*, 159–168.
- 734 (31) Qiao, J. S.; Kong, X. H.; Hu, Z. X.; Yang, F.; Ji, W. High-  
735 Mobility Transport Anisotropy and Linear Dichroism in Few-Layer  
736 Black Phosphorus. *Nat. Commun.* **2014**, *5*, 4475.
- 737 (32) Terrones, H.; Lopez-Urias, F.; Terrones, M. Novel Hetero-  
738 Layered Materials with Tunable Direct Band Gaps by Sandwiching  
739 Different Metal Disulfides and Diselenides. *Sci. Rep.* **2013**, *3*, 1549.
- 740 (33) Tongay, S.; Zhou, J.; Ataca, C.; Lo, K.; Matthews, T. S.; Li, J.  
741 B.; Grossman, J. C.; Wu, J. Q. Thermally Driven Crossover from  
742 Indirect toward Direct Bandgap in 2D Semiconductors: MoSe<sub>2</sub> versus  
743 MoS<sub>2</sub>. *Nano Lett.* **2012**, *12*, 5576–5580.
- 744 (34) Datta, S. S.; Strachan, D. R.; Mele, E. J.; Johnson, A. T. C.  
745 Surface Potentials and Layer Charge Distributions in Few-Layer  
746 Graphene Films. *Nano Lett.* **2009**, *9*, 7–11.
- 747 (35) Gao, T.; Song, X. J.; Du, H. W.; Nie, Y. F.; Chen, Y. B.; Ji, Q.  
748 Q.; Sun, J. Y.; Yang, Y. L.; Zhang, Y. F.; Liu, Z. F. Temperature-  
749 Triggered Chemical Switching Growth of in-Plane and Vertically  
750 Stacked Graphene-Boron Nitride Heterostructures. *Nat. Commun.*  
751 **2015**, *6*, 6835.
- 752 (36) Hong, X. P.; Kim, J.; Shi, S. F.; Zhang, Y.; Jin, C. H.; Sun, Y. H.;  
753 Tongay, S.; Wu, J. Q.; Zhang, Y. F.; Wang, F. Ultrafast Charge  
754 Transfer in Atomically Thin MoS<sub>2</sub>/WS<sub>2</sub> Heterostructures. *Nat.*  
755 *Nanotechnol.* **2014**, *9*, 682–686.
- 756 (37) Kresse, G.; Joubert, D. From Ultrasoft Pseudopotentials to the  
757 Projector Augmented-Wave Method. *Phys. Rev. B: Condens. Matter*  
758 *Mater. Phys.* **1999**, *59*, 1758–1775.
- 759 (38) Blochl, P. E. Projector Augmented-Wave Method. *Phys. Rev. B:*  
760 *Condens. Matter Mater. Phys.* **1994**, *50*, 17953–17979.
- 761 (39) Monkhorst, H. J.; Pack, J. D. Special Points for Brillouin-Zone  
762 Integrations. *Phys. Rev. B* **1976**, *13*, 5188–5192.
- 763 (40) Dion, M.; Rydberg, H.; Schroder, E.; Langreth, D. C.;  
764 Lundqvist, B. I. Van Der Waals Density Functional for General  
765 Geometries. *Phys. Rev. Lett.* **2004**, *92*, 246401.
- 766 (41) Klimes, J.; Bowler, D. R.; Michaelides, A. Van Der Waals  
767 Density Functionals Applied to Solids. *Phys. Rev. B: Condens. Matter*  
768 *Mater. Phys.* **2011**, *83*, 195131.
- 769 (42) Hu, Z. X.; Lan, H. P.; Ji, W. Role of the Dispersion Force in  
770 Modeling the Interfacial Properties of Molecule-Metal Interfaces:  
771 Adsorption of Thiophene on Copper Surfaces. *Sci. Rep.* **2015**, *4*, 5036.
- 772 (43) Wu, J. B.; Hu, Z. X.; Zhang, X.; Han, W. P.; Lu, Y.; Shi, W.;  
773 Qiao, X. F.; Ijias, M.; Milana, S.; Ji, W.; Ferrari, A. C.; Tan, P. H.  
774 Interface Coupling in Twisted Multilayer Graphene by Resonant  
775 Raman Spectroscopy of Layer Breathing Modes. *ACS Nano* **2015**, *9*,  
776 7440–7449.